Smart Agricultural Technology 7 (2024) 100434

Contents lists available at ScienceDirect

Smart Agricultural Technology

journal homepage: www.journals.elsevier.com/smart-agricultural-technology

Precision viticulture: Automatic selection of the regions of interest from moving wagon hyperspectral images of grapes for efficient SSC prediction

Alessandro Benelli [a,b,*], Chiara Cevoli [b], Angelo Fabbri [b], Søren Balling Engelsen [c], Klavs Martin Sørensen [c]

[a] Department for Innovation in Biological, Agro-Food and Forest Systems, University of Tuscia, Via San Camillo de Lellis snc, Viterbo 01100, Italy
[b] Department of Agricultural and Food Sciences, Alma Mater Studiorum, University of Bologna, Piazza Goidanich 60, Cesena 47521, Italy
[c] Food Analytics & Biotechnology, Department of Food Science, University of Copenhagen, Rolighedsvej 26, Frederiksberg 1958, Denmark

ARTICLE INFO

Keywords:
Hyperspectral imaging
Grape
Automatic
Classification
PLS-DA
PLS

ABSTRACT

Precision viticulture is increasingly being applied to automate and optimize grape production in the vineyard. This paper describes the development of a method for automatic selection of regions of interest from hyperspectral images obtained of a row of vines and intended for prediction of soluble solids content. For this purpose, a dataset consisting of hyperspectral images of a row of 'Sangiovese' wine grapes was adopted. Hyperspectral images were acquired directly in the field by means of a hyperspectral imaging Vis/NIR system (400–1000 nm) mounted on a ground-based vehicle. The analyses were carried out on 17 different days, under clear or partly cloudy conditions, in the period between post-veraison and harvest. The vineyard row of Sangiovese vines was divided into 11 sections and a hyperspectral image for each section for each day of analysis was acquired. The regions of interest of the hyperspectral images, comprising the areas representing the grapes, were selected using a PLS-DA-based method. The best PLS-DA model provided excellent results, with sensitivity and specificity values of 0.991 and 0.996, respectively. The mean spectra of the selected regions of interest (ROI) were finally used to predict the soluble solids content (SSC) of the grapes by PLS regression to a primary reference analysis. The results of SSC predictions using the automatic selection of ROIs ($R^2_{CV} = 0.74$ and RMSECV = 0.86 °Brix) were on par with similar regression based on carefully manual selection of ROIs ($R^2_{CV} = 0.73$ and RMSECV = 0.87 °Brix).

1. Introduction

Vines are one of the most important crops in Europe, playing a key environmental and socio-economic role [1]. In particular, the Mediterranean area is world leading in wine production. In 2021, Italy, Spain and France together accounted for 79 % of EU wine production, while on a global scale they reached 45 % [2]. Italy has the first place with a production of 44.5 million hectolitres (MhL), followed by Spain with 35.0 MhL and France with 34.2 MhL [2].

As all other agricultural products, the wine sector is strongly influenced by the ongoing global climate change. The global rise in temperature is caused by the increase in atmospheric CO_2 originating from human activity [3]. Specific thermal and hydrologic conditions are the two most frequently cited factors in arguments regarding the potential effects of climate change on viticulture [1]. In addition, the angle of penetration of solar radiation into the canopies also affects grape temperature and composition [4]. Water-saving irrigation methods based on vine physiology, such as regulated deficit irrigation, partial root zone drying irrigation, and subsurface drip irrigation strategies, are essential for improving both water efficiency as well as berry and wine quality. Furthermore, in order to design agricultural systems, including vineyards, that are sustainable and resilient to climate change,

Abbreviations: R^2, coefficient of determination; R^2_{cv}, coefficient of determination of cross validation; R^2_p, coefficient of determination of prediction; EMSC, extended multiplicative scatter correction; HS, hyperspectral; HSI, hyperspectral imaging; *i*PLS, interval partial least squares; MC, mean centring; MhL, million hectolitres; MS, multispectral; PLS, partial least squares; PLS-DA, partial least squares discriminant analysis; PA, precision agriculture; PV, precision viticulture; *r*PLS, recursive weighted partial least squares; ROIs, regions of interest; RMSE, root-mean-square error; RMSECV, root-mean-square error of cross validation; RMSEP, root-mean-square error of prediction; SWIR, short-wave infrared; SW-NIR, short-wave near-infrared; SSC, soluble solids content; SNV, standard normal variate; SVM, support vector machines; TIR, thermal infrared; TSS, total soluble solids; UAVs, unmanned aerial vehicles; Vis, visible; Vis/NIR, visible/near-infrared.

* Corresponding author at: Via San Camillo de Lellis snc, Viterbo 01100, Italy.
E-mail address: alessandro.benelli@unitus.it (A. Benelli).

https://doi.org/10.1016/j.atech.2024.100434
Received 27 December 2023; Received in revised form 6 March 2024; Accepted 6 March 2024
Available online 7 March 2024

sustainable soil management practices such as cover crops, mulching, composting, reduced tillage, mutualistic plant-microorganism interactions, and agroforestry could be implemented [5].

Future climate changes could make new areas suitable for vine cultivation, require significant movement within current growing areas, affect the phenological timing of vines, and eventually alter the composition of grapes and wine [1]. An already evident effect of climate change is the tendency to anticipate and accelerate the phenological phases flowering, veraison and harvest. The period between budbreak and harvest tends to shorten and ripening to move toward the warmer part of the growing season of grapes. If ripening occurs earlier, there is less time for the pre-veraison synthesis of organic acids and flavanols, which can be also precursors of tannins. In addition, an early and rapid accumulation of sugars occurs during ripening, which is not necessarily coupled with the accumulation of anthocyanin pigments and aromatic components. This can lead to a decision to delay the harvest, resulting in wines with increasingly higher alcohol contents [6].

In the mid-1980s, the concept of precision agriculture (PA) was introduced [7]. PA is a method of agricultural, forestry and livestock management based on the observation, measurement, and response of the set of quantitative and qualitative inter- and intra-field variables acting in agricultural production. The purpose of PA is to define a decision support system for the entire farm management, with the aim of optimising yields while looking at climatic, environmental, economic, productive, and social sustainability [8]. PA involves the collection of data through proximal or remote sensors installed on variable rate technology systems, which carry out the given tasks in a semi- or fully automatic way. The assumption behind PA is that each field, unlike how it is generally considered in conventional agriculture, is not uniform, but is managed considering site-specific characteristics. This management strategy increases the efficiency of agricultural inputs and, if adopted correctly, results in cost savings and increased benefits [8]. The concept of precision viticulture (PV) is based on PA. In the same vineyard, there are usually several areas with different soil composition and structure, humidity concentration, sun exposure and microclimate. Consequently, the objectives of PV, *i.e.*, the assessment of the health, vigour, and physiological needs of the vines, are related to the different areas of the vineyard over time, which results in a specific adaptation of cultivation techniques. In addition, one of the objectives of PV is the monitoring of grape bunches during ripening. The data collected may concern the degree of ripeness, sugars (expressed as soluble solids content), anthocyanins, acidity, growth ratio. This monitoring can be aimed at selective grape harvesting, which will affect the quality of the wine [8].

Remote sensing systems for data collection are characterised by optical sensors such as RGB visible (Vis) cameras, multispectral (MS) and hyperspectral (HS) sensors, thermal infrared (TIR) sensors, and other spectroscopic sensors like D-radar, Vis, short-wave infrared (SWIR), short-wave near-infrared (SW-NIR). Remote sensing technologies involve the use of satellites, aircraft, and unmanned aerial vehicles (UAVs) or drones [9,10]. Their introduction has taken place in the last decade but has faced major challenges due to the organisation of the vineyard in rows and the discontinuous nature of the canopy. These characteristics require a high capacity for processing images, which must have a very high resolution to discriminate the canopy from the ground, and spatial data [8].

Among the most analysed attributes by remote sensing systems are vine vigour, water stress, and more recently also some diseases. Vine vigour was assessed through MS imaging [11]. Vine vigour, obtained from RGB and MS imaging, was also correlated to yield, berry composition and vine sanitary status [12]. Vine vigour and water stress of vines were correlated and validated through RGB, MS and TIR imaging [13–15]. Water stress maps were obtained by comparing vine vigour obtained from SWIR and MS imaging, with leaf stomatal conductance measurements [16]. MS imaging data has also been combined with a decision-making vine water consumption model in order to optimise irrigation [17]. Water stress assessed by TIR imaging has been compared with traditional vine water status metrics [18]. MS imaging has been adopted to evaluate status of flavescence dorée grapevine disease [19,20] and grape trunk disease [20]. Flavescence dorée has also been evaluated through RGB imaging [21].

Proximal sensing systems can be implemented on ground vehicles monitoring of quality attributes of grape ripening, such as soluble solids content (SSC) and acidity directly in the field. The hyperspectral imaging (HSI) sensors recently adopted can operate at short distance from the vineyard row and due to the high resolution, the bunches of grapes can be easily manually discriminated from the background. An on-the-go HSI system was adopted to estimate the concentration of SSC (coefficient of determination (R^2) = 0.92, root-mean-square error (RMSE) = 1.274 °Brix) and anthocyanins (R^2 = 0.83, RMSE = 0.211 mg g^{-1}) of wine grapes by support vector machines (SVM) [22]. Fernández-Novales et al. [23] and Fernández-Novales et al. [24] acquired hyperspectral images of grape cluster regions along vineyard rows during the period between veraison and harvest. Hyperspectral images were acquired directly in the field using an on-the-go HSI system operating in the 570–990 nm spectral range. The best results obtained from partial least squares regression (PLS) regression models consisted of R^2 of prediction (R^2_p) = 0.95 for total soluble solids (TSS), R^2_p = 0.88 for anthocyanins. The accuracy of the models, expressed in terms of root-mean-square error of prediction (RMSEP), resulted in RMSEP = 1.01 °Brix for TSS, RMSEP = 0.20 mg/fresh berry mass for anthocyanins. In another study, the proper maturity of red wine grapes after veraison and up to harvest (through SSC) was assessed by adopting a cart mounted HSI system. By PLS the SSC was predicted (R^2 = 0.77, RMSECV = 0.79 °Brix) and by partial least squares discriminant analysis (PLS-DA) the samples were

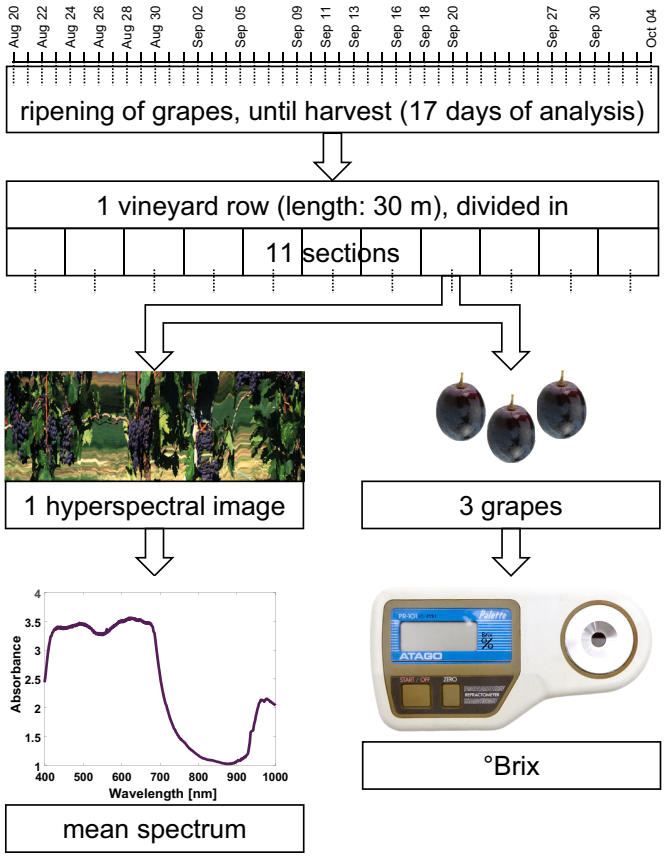

Fig. 1. During 17 days of analysis, 187 hyperspectral images of a vineyard row divided into 11 sections were acquired (1 hyperspectral image per section per day of analysis), obtaining 187 mean absorbance spectra; soluble solids content, expressed in °Brix, of 561 grape berries were analysed (3 grape berries per section per day of analysis) by means of a digital refractometer.

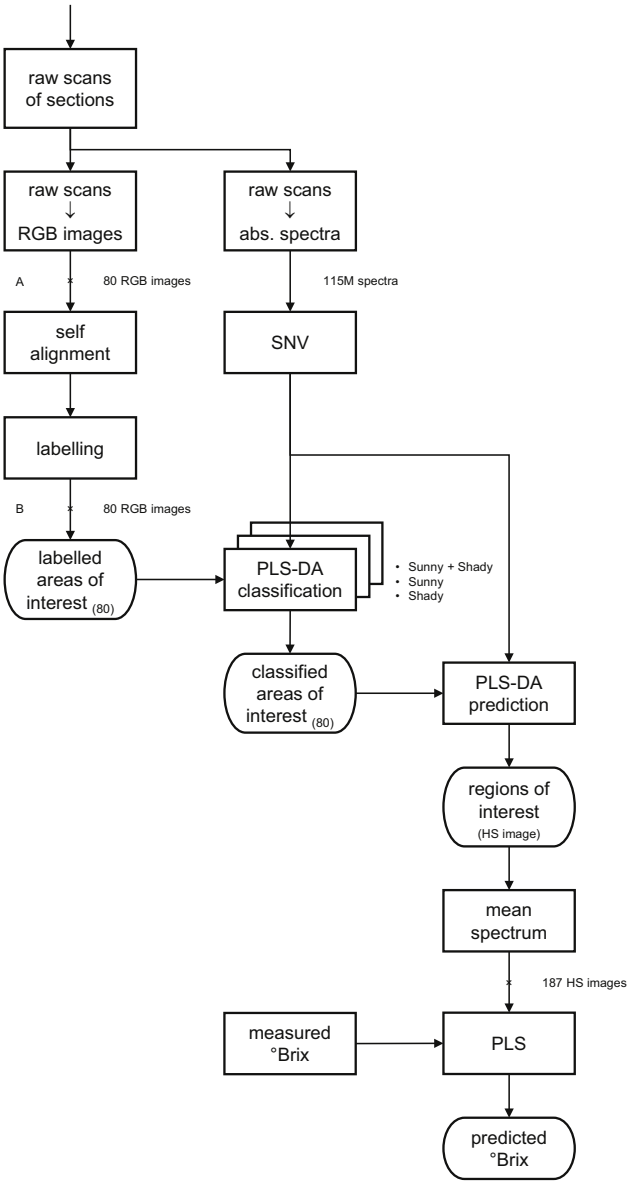

Fig. 2. Data flow, from the acquisition of the hyperspectral images of the sections of a vineyard row, to the prediction of °Brix of the grapes.

classified in the two classes 'not-ripe' and 'ripe' (correctly classified samples from 86 % to 91 %) [25].

A main challenge in the use of optical techniques for the determination of grape quality attributes from HSI is how to define and select the pixels containing the grape clusters from the images acquired [26]. The aim of this study is to develop a method for the pixel-based automatic selection of grapes, which represent the regions of interest (ROIs) of the hyperspectral images of a row of wine grapes acquired in the field during post-harvest and up to harvest. The study is based on hyperspectral data from Benelli et al. [25] acquired under clear sky conditions, integrated with hyperspectral data acquired under partly cloudy conditions. The selection method include bias from the natural lighting conditions of the grapes and is able to distinguish grapes in the sun and grapes in the shade. The selected ROIs were subsequently used to predict the SSC of the grapes.

2. Materials and methods

2.1. Samples

The analysis covered approximately 30 m of one side of a vineyard row of red 'Sangiovese' grapes (*Vitis vinifera* L.), located near Cesena, Italy. The vineyard row was analysed on 17 different days between August 20th and October 4th, 2019, from post-veraison to harvest time. At this stage, the skin of the berry is dark in colour as a result of the progressive accumulation of red, purple or blue anthocyanin pigments and degradation of green chlorophyll; in addition, accumulation of sugars (glucose, fructose) occurs. The degree and balance in the accumulation of these substances is critical for the grape maturity and thus optimal harvest time [6]. The vine's topping was only partially completed to intentionally shade some bunches, in accordance with the work's objectives. The row was divided into 11 sections, and from each section, three grapes were taken for each day for reference analysis,

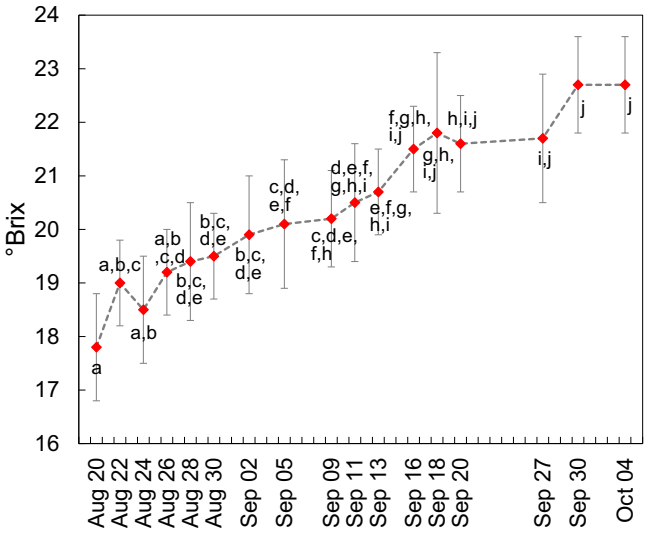

Fig. 3. Means (filled red diamonds) and standard deviations (grey bars) of soluble solids content (SSC, expressed in °Brix) during the 17 days of analysis. Means with the same letter are not significant different at p-level < 0.05.

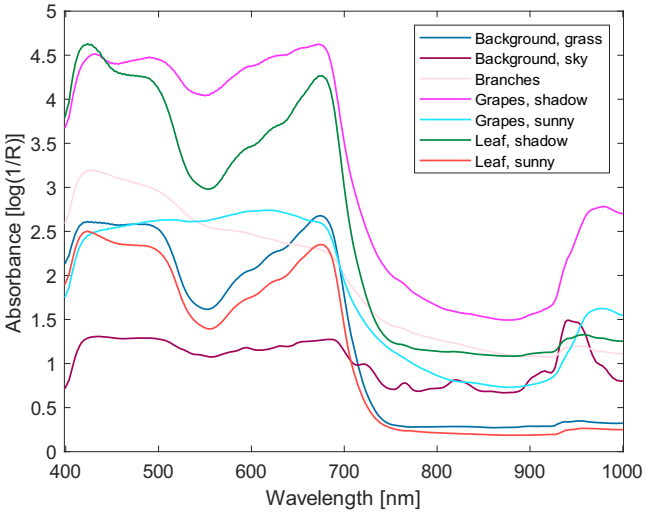

Fig. 4. Mean calibrated diffuse absorbance (for brevity 'absorbance' in the figure) spectra of the seven classes of labelled areas of interest ('Background, grass', 'Background, sky', 'Branches', 'Grapes, shadow', 'Grapes, sunny', 'Leaf, shadow', 'Leaf, sunny'), obtained by averaging the respective mean spectra of all labelled areas of interest (2506).

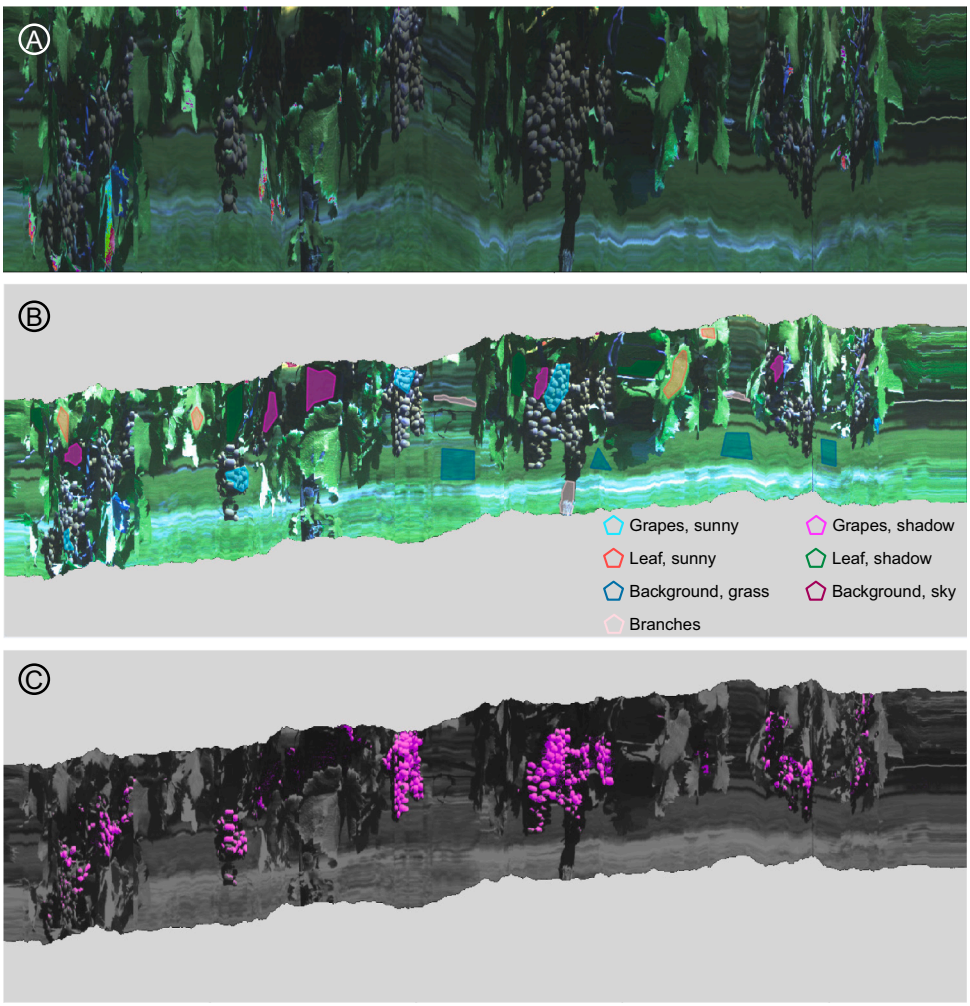

Fig. 5. Representations of a single scan. (A) The raw scan as a false-colour image where R = 680 nm, G = 520 nm and B = 460 nm. (B) Aligned for vertical movement, same false colour representation as (A) with gamma = 2.2 applied for visibility. The coloured polygons are the manually labelled classes, where cyan is grapes (sunny), magenta is grapes (shadow), orange is leaf (sunny), green is leaf (shadow), blue is background (grass), purple is background (sky), and pink is branches. (C) Grey scale representation of the scan, with the pixels highlighted in magenta identified by the 'Sunny + Shady' selected PLS-DA classification model using the 'Super' classification threshold.

giving a total of 561 grape samples (Fig. 1). Due to adverse weather conditions, it was not possible to carry out the analyses on certain dates, which is why there are natural discontinuities in the experimental timeline (Fig. 1).

2.2. Hyperspectral images acquisitions

The study was conducted using a line scan hyperspectral camera (Nano-Hyperspec VNIR, Headwall Photonics, Inc., Fitchburg, MA, USA), operating in the visible/near-infrared (Vis/NIR) spectral range (400–1000 nm). The camera is characterized by 272 spectral pixels, with a nominal spectral resolution of 2.2 nm. The used lens (Xenoplan 1.4/17–0903, Schneider-Kreuznach, GmbH, Bad Kreuznach, Rhineland-Palatinate, Germany) presents an effective focal length of 17 mm. The camera was installed on a garden cart, at a height of 120 cm above the ground, and was driven at approximately 1.6 m from the vineyard row analysed. The choice of this type of hyperspectral image acquisition mode is to mimic its implementation on a vineyard tractor.

Hyperspectral image acquisitions were carried out between 10:30 and 12:00. Direct sunlight was used as light source under both clear sky (14 days) and partly cloudy (3 days) conditions. Depending on the light intensity, the exposure time was set between 6 and 8 ms in clear sky conditions, and between 8 and 25 ms in partly cloudy conditions. The exposure time was obtained through calibration with a panel of broadband high-reflectance white target (hardboard coated with white matte finish paint), positioned close to the vineyard row, perpendicular to the main optical axis, covering the entire angle of view of the camera. The integration time was determined as the exposure time (ms) yielding a maximum pixel intensity return (approximately 3000 counts) from the white target.

Under clear sky conditions, calibration was carried out only once a day, as the acquisition of hyperspectral images of the 11 vineyard row sections required no more than 10 min. Under partly cloudy conditions, a calibration was necessary for each acquisition, due to the variability of the intensity of light radiation. This situation extended the analysis time considerably.

A total of 187 hyperspectral images were obtained, one per section of the vineyard row per day of analysis (11 sections × 17 days of analysis = 187 hyperspectral images). From the raw diffuse reflectance spectra (R_R) extracted from the hyperspectral images, the calibrated diffuse reflectance spectra (R_C) were calculated by applying the equation [27]:

$$R_C = \frac{R_R - R_D}{R_W - R_D} \quad (1)$$

where R_D is the dark reference reflectance spectrum, obtained applying the cap on the lens; R_W are the white reference reflectance spectra,

Table 1
PLS-DA models to discriminate the grapes ('Sunny + Shady', 'Sunny', and 'Shady' grape classes) from the background (obtained aggregating the remaining classes, except 'Background, sky'). The best PLS-DA models are highlighted in italics.

Aggregated grape class	Pre-processing	All variables /*i*PLS int. size	# LVs	Sensitivity (CV)	Specificity (CV)
Sunny + Shady	SNV	All	4	0.994	0.996
	SNV	6	3	0.986	0.996
	SNV	12	6	0.994	0.996
	SNV	25	4	0.992	0.995
	SNV	*50*	*3*	*0.991*	*0.996*
	D1	All	3	0.992	0.995
	D1	6	2	0.990	0.985
	D1	12	8	0.992	0.996
	D1	25	4	0.988	0.996
	D1	50	4	0.990	0.996
	D2	All	3	0.988	0.985
	D2	6	4	0.991	0.990
	D2	12	3	0.987	0.991
	D2	25	4	0.985	0.991
	D2	50	3	0.985	0.994
	Detrend	All	5	0.992	0.997
	Detrend	6	5	0.991	0.996
	Detrend	12	4	0.987	0.995
	Detrend	25	6	0.994	0.995
	Detrend	50	3	0.986	0.997
	EMSC	All	3	0.992	0.979
	EMSC	6	5	0.994	0.974
	EMSC	12	5	0.992	0.974
	EMSC	25	3	0.988	0.960
	EMSC	50	5	0.990	0.969
Sunny	*SNV*	*6*	*4*	*0.988*	*0.940*
Shady	*SNV*	*6*	*9*	*0.920*	*0.927*

Pre-processing methods details. SNV (standard normal variate): smoothing, window = 9 + SNV + MC (mean centring). D1 (Savitzky-Golay first derivative): D1, smoothing window = 7, polynomial order = 2 + MC; D2 (Savitzky-Golay second derivative): D2, smoothing window = 15, polynomial order = 2 + MC. Detrend: smoothing, window = 31 + detrend, polynomial order = 1 + MC. EMSC (extended multiplicative scatter correction): smoothing, window = 15 + EMSC + MC. *i*PLS int. size: *i*PLS interval size. # LVs: number of latent variables. CV: leave-one-section-out cross-validation.

obtained by the above-described white calibration.

Each R_C were finally converted in calibrated diffuse absorbance spectra (A_C) [28]:

$$A_C = log\frac{1}{R_C} \quad (2)$$

2.3. Soluble solids content measurement

SSC, expressed in °Brix, was measured with a portable digital refractometer (PR-101 Digital Refractometer, ATAGO CO., LTD, Tokyo, Japan) by taking three randomly selected grapes from each of the 11 vineyard row sections for each day of analysis (Fig. 1). °Brix values are a measure of the SSC of a solution; sugars are the most abundant soluble solids in grapes. The mean of the °Brix for each section was calculated. Through one-way analysis of variance (ANOVA) with Tukey-HSD post-hoc test (p-level < 0.05), significant differences between the mean of SSC for the days of analysis were evaluated.

2.4. Hyperspectral images elaboration

2.4.1. RGB images extraction and labelling

An RGB image was extracted from each hyperspectral image, resulting in 187 RGB images. The vertical scan lines forming the RGB images were aligned using a self-alignment algorithm. The image canvas was extended with 150 pixels above and below the scan line data. Then, for each of the scan lines, the neighbour vertical line was shifted by the self-alignment algorithm from 30 pixels up to 30 pixels down and the RMSE of the grey pixel values between the two lines were determined for each step (61 steps in total). The chosen shift was selected as the one that yielded the lowest RMSE and applied to all subsequent scans comprising the image, and then the next scan line was processed in the same way. The process was repeated for all scan lines in the image (see Fig. 5).

A total of 80 RGB images randomly selected were then manually labelled using the Labelbox® web tool [29]. The self-aligned RGB images were manually labelled by assigning 7 different labelling classes: 'Grapes, sunny', 'Grapes, shadow', 'Leaf, sunny', 'Leaf, shadow', 'Background, grass', 'Background, sky', 'Branches'. Labelling was done coarsely by drawing polygons around relevant areas in the images. At least four areas of each class were selected in all the 80 RGB images, resulting in a total of 2506 areas of interest. Absorbance spectra for the areas of interest were extracted from the hyperspectral images as the pixel values circumscribed by the label polygons. Finally, a mean absorbance spectrum was calculated for each selected area, resulting in 2506 labelled mean spectra. The whole flow of the data processing is

Table 2
Results of PLS models obtained by adopting the different classes of regions of interest ('Sunny + shady', 'Sunny', 'Shady', 'Super Sunny + Shady', 'Super Sunny', 'Super Shady', 'Manual' selection) and applying the reported pre-processing (SNV and Savitzky-Golay second derivative) and cross-validation methods (leave-one-day out and leave-one-section out). The best PLS models are highlighted in italics.

ROIs	Prepro.	#LV	R^2_{cal}	R^2_{CV}	RMSEC	RMSECV	#LV	R^2_{cal}	R^2_{CV}	RMSEC	RMSECV
		Leave-one-day out cross-validation					Leave-one-section out cross-validation				
Sunny + Shady	*SNV*	*5*	*0.73*	*0.69*	*0.87*	*0.94*	5	0.73	0.69	0.87	0.94
	2D	5	0.71	0.58	0.91	1.09	4	0.65	0.56	1.00	1.13
Sunny	SNV	6	0.61	0.51	1.06	1.19	6	0.61	0.49	1.06	1.22
	2D	6	0.63	0.45	1.03	1.27	8	0.68	0.59	0.96	1.09
Shady	SNV	9	0.80	0.67	0.75	0.97	8	0.79	0.71	0.77	0.92
	2D	3	0.62	0.53	1.05	1.16	3	0.62	0.56	1.05	1.13
Super Sunny + Shady	*SNV*	*4*	*0.73*	*0.67*	*0.88*	*0.97*	5	0.73	0.69	0.87	0.95
	2D	5	0.67	0.55	0.97	1.14	4	0.63	0.55	1.02	1.14
Super Sunny	SNV	8	0.51	0.30	1.18	1.43	8	0.51	0.37	1.18	1.36
	2D	8	0.60	0.33	1.07	1.41	7	0.57	0.43	1.10	1.29
Super Shady	SNV	9	0.81	0.67	0.74	0.97	8	0.79	0.71	0.77	0.92
	2D	3	0.61	0.51	1.05	1.18	3	0.61	0.55	1.05	1.14
Manual	*SNV*	*7*	*0.76*	*0.70*	*0.83*	*0.92*	3	0.70	0.66	0.92	0.98
	2D	6	0.73	0.66	0.87	0.98	3	0.69	0.63	0.94	1.03

ROIs: regions of interest; Prepro.: pre-processing method; #LV: number of latent variables; CV: cross-validation; SNV: standard normal variate; 2D: Savitzky-Golay second derivative, smoothing window = 19, polynomial order = 2.

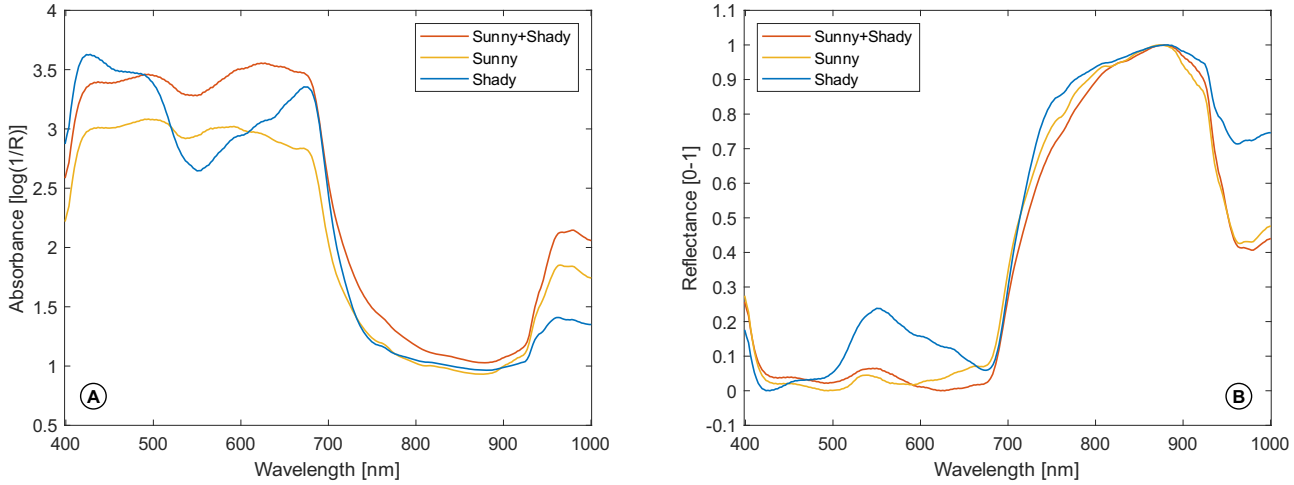

Fig. 6. (A) Mean calibrated diffuse absorbance (for brevity 'absorbance' in the figure) spectra and (B) mean calibrated diffuse reflectance (for brevity 'reflectance' in the figure) spectra normalized in the 0–1 reflectance range. The spectra represent the three defined classes of grapes (Sunny+Shady, Sunny, Shady) and are obtained by averaging the mean spectra of the whole dataset of hyperspectral images (187).

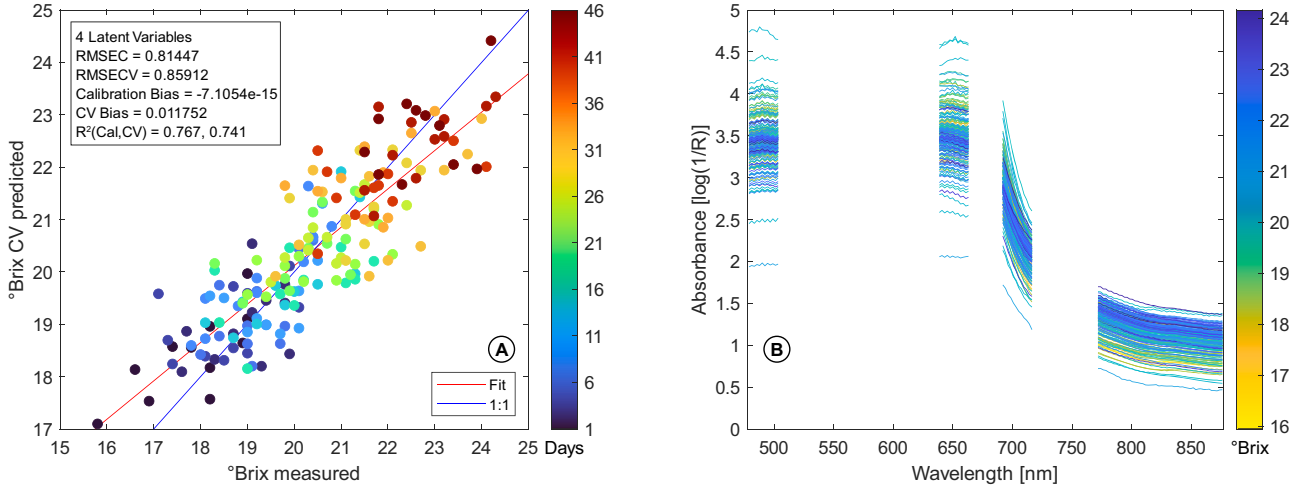

Fig. 7. (A) Measured *vs* predicted values of soluble solids content (°Brix) from the best PLS regression model for the Sunny+Shady grape class (cross-validation: leave-one-day out). The 'Fit' line (in red) represents the linear regression line of the PLS model. In the '1:1' line (in blue), the observed °Brix values are equal to those predicted by the PLS model. (B) Spectral bands (84 wavelengths) resulting from the *i*PLS variable selection method and used in the best PLS regression model for the Sunny+Shady grape class. For brevity, the calibrated diffuse absorbance is reported as 'absorbance'.

outlined in Fig. 2.

2.4.2. *Automatic classification*

The analyses were carried out by PLS Toolbox (PLS_Toolbox, 2020. Eigenvector Research, Inc., Manson, WA, USA) for MATLAB (MATLAB R2020b, The MathWorks, Inc., Natick, Massachusetts, USA) software. PLS-DA [30] was adopted to classify the mean spectra obtained from the labelling of the 80 randomly selected RGB images.

In order to discriminate the grapes from the background, 'Grapes, sunny' and 'Grapes, shadow' classes were combined in the 'Sunny + Shady' aggregated grape class; therefore, the classes 'Leaf, sunny', 'Leaf, shadow', 'Background, grass', and 'Branches' were combined, obtaining the 'Background' aggregated class. The 'Background, sky' class was excluded due to the high heterogeneity of its mean spectra. The mean spectra were pre-processed by the following methods: smoothing (window: 9) + standard normal variate (SNV), smoothing (window: 31) + detrend (polynomial order: 1, to remove linear offset), smoothing (window: 15) + extended multiplicative scatter correction (EMSC), Savitzky-Golay first derivative (smoothing window: 7; polynomial order: 2), and second derivative (smoothing window: 15; polynomial order: 2), all followed by mean centring (MC) [31]. Subsequently, the interval PLS (*i*PLS) method for variable region selection was applied, testing 4 different interval sizes (6, 12, 25, 50) in 'forward' mode, with non-overlapping intervals subsequently and automatically included in the analysis [32]. This approach is useful for variable selection and thus omitting irrelevant spectral data from interfering compounds, typically leading to more parsimonious and robust models. The PLS-DA models were validated by leave-one-section-out cross-validation ('section' refers to a single hyperspectral image of a vineyard section, see Fig. 1). Only PLS-DA models with sensitivity (number of samples predicted as class members divided by the actual number of class members) and specificity (number of samples predicted as non-class members divided by the actual number of non-class members) values for the aggregated class 'Sunny + Shady' greater than or equal to 0.99 were considered. Finally, the PLS-DA model that simultaneously showed the lowest number of latent variables and the highest sensitivity or specificity value for the 'Sunny + Shady' aggregated class was selected. PLS tries to find latent variables that maximise the amount of variation in the spectra that is relevant for predicting SSC content. The number of latent variables is validated by cross validation or preferably test set validation.

Table 3
PLS models obtained by adopting the ROIs and the settings (SNV pre-processing and leave-one-day out cross-validation methods) of the three best PLS models reported on Table 2 (rows in italics), and two variable selection methods (*i*PLS and *r*PLS). The best PLS models are highlighted in italics.

ROIs	Var. sel. method	*i*PLS window/*r*PLS mode	#LV	#var.	R^2_{cal}	R^2_{CV}	RMSEC	RMSECV
Sunny+Shady	–	–	*5*	*All*	*0.73*	*0.69*	*0.87*	*0.94*
	*i*PLS	6	9	23	0.78	0.73	0.79	0.88
	iPLS	*12*	*4*	*84*	*0.77*	*0.74*	*0.81*	*0.86*
	*i*PLS	25	6	49	0.79	0.74	0.78	0.86
	*i*PLS	50	3	99	0.73	0.69	0.88	0.94
	*r*PLS	surveyed	7	29	0.75	0.66	0.85	0.98
	*r*PLS	specified 5 LV	4	72	0.74	0.70	0.86	0.92
	*r*PLS	suggested	3	17	0.73	0.69	0.88	0.94
Super Sunny+Shady	–	–	*4*	*All*	*0.73*	*0.67*	*0.88*	*0.97*
	*i*PLS	6	5	12	0.75	0.70	0.84	0.92
	*i*PLS	12	7	36	0.79	0.75	0.78	0.84
	iPLS	*25*	*5*	*49*	*0.77*	*0.74*	*0.80*	*0.86*
	*i*PLS	50	4	50	0.75	0.71	0.85	0.91
	*r*PLS	surveyed	7	25	0.76	0.63	0.83	1.04
	*r*PLS	specified 4 LV	5	28	0.72	0.69	0.89	0.97
	*r*PLS	suggested	5	28	0.72	0.69	0.89	0.97
Manual	–	–	*7*	*All*	*0.76*	*0.70*	*0.83*	*0.92*
	iPLS	*6*	*6*	*48*	*0.76*	*0.73*	*0.83*	*0.87*
	*i*PLS	12	3	108	0.72	0.70	0.90	0.93
	*i*PLS	25	6	100	0.76	0.71	0.82	0.91
	*i*PLS	50	6	100	0.76	0.71	0.82	0.91
	*r*PLS	surveyed	3	27	0.68	0.60	0.96	1.07
	*r*PLS	specified 7 LV	4	13	0.65	0.56	1.00	1.13
	*r*PLS	suggested	1	19	0.69	0.67	0.94	0.96

ROIs: regions of interest; Var. sel. method: variable selection method; #LV: number of latent variables; #var.: number of variables; *i*PLS: interval PLS; *r*PLS: recursive weighted PLS.

Afterwards, the two classes 'Grapes, sunny' and 'Grapes, shadow' (renamed to 'Sunny' and 'Shady', respectively) were considered individually in order to discriminate grapes exposed directly to the sun and grapes in the shadow from their respective backgrounds.

The same pre-processing as for the PLS-DA classification model selected for the aggregated class 'Sunny + Shady' was used to calculate the new PLS-DA classification models, then variable selection was performed using the same *i*PLS method (interval sizes: 6, 12, 25, 50) described above. Finally, the two best PLS-DA classification models for the 'Sunny' and 'Shady' classes respectively were selected in terms of best performance for sensitivity, specificity, and low number of latent variables (Fig. 2).

2.4.3. Regions of interest of the hyperspectral images

The three previously selected PLS-DA classification models (related to grape classes 'Sunny + Shady', 'Sunny, and 'Shady') were then adopted to predict the pixel-based ROIs of the whole hyperspectral image set (187). Each class of ROI would include spectra attributed to the three grape classes 'Sunny + Shady', 'Sunny', and 'Shady', respectively. Two different set of classification threshold where tested, one at 50 % of the predicted values and one at 90 % of the predicted values (the 'Super' threshold). Ergo, a total of six classes were obtained: 'Sunny + Shady', 'Sunny' and 'Shady' for the first threshold, 'Super Sunny + Shady', 'Super Sunny' and 'Super Shady' for the second threshold (Fig. 2).

2.4.4. Soluble solids content of grapes prediction

The mean absorbance spectra relative to each ROIs class were calculated for each of the 187 hyperspectral images, resulting in six mean spectra (one per ROI class) for each hyperspectral image.

PLS models were built for each of the ROIs classes to predict the SSC of the grapes (in °Brix), using the 187 mean spectra that characterise each class. Two pre-processing methods, SNV and Savitzky-Golay second derivative (smoothing window: 19; polynomial order: 2), both followed by MC, were used to calculate PLS models; models were validated by leave-one-day-out and leave-one-section-out cross-validation.

Finally, the resulting PLS models were compared with PLS models obtained by manual selection of ROIs [25]. The metrics used to describe the results of the PLS models are R^2 and RMSE.

$$R^2 = 1 - \frac{\sum_i (y_i - \hat{y}_i)^2}{\sum_i (y_i - \bar{y})^2} \quad (3)$$

where y_i is the measured °Brix value, $\hat{y}_i$ is the predicted value, and $\bar{y}$ is the mean value. The squared coefficient of determination (R^2) describes the variance explained. An R^2 of 1 indicates that the regression predictions are perfectly correlated to the measured variables.

$$RMSE = \sqrt{\frac{\sum_{i=1}^{n_p} (\hat{y}_i - y_i)^2}{n_p}} \quad (4)$$

where n_p is the number of samples. The root-mean-square error (RMSE) measures the differences between sample values predicted by the PLS model and the observed values, and provide a measure of the expected prediction error of the model.

The best PLS models, in terms of number of latent variables, R^2_{CV} and RMSECV, were selected and recalculated by adopting two variable selection methods, *i*PLS and recursive weighted partial least squares (*r*PLS) [33] (Fig. 2).

3. Results and discussion

Mean values of the SSC and standard deviations by day of analysis are reported in Fig. 3. The SSC ranged from 17.8 °Brix on the first day of analysis (August 20) to 22.7 °Brix during the last day of analysis (October 4), which represents a rise of 27.5 %. Significant differences were found between the mean °Brix values for the days of analysis. Due to adverse weather conditions, *i.e.*, rain or extensive cloud cover, it was not possible to carry out in-field analyses at regular time intervals: this occurred several times between September 20 and September 27.

Automatic methods for selecting ROIs in hyperspectral images of vineyards and grapes are often based on visual image analysis, namely colour and geometry [34–36]. The use of HSI (Vis/NIR spectra) provides additional chemical/physical information which can be exploited to select ROIs that not only looks alike but also contains same chemical information. This approach thus improves the selection of ROIs, by

making the selection less prone to errors stemming from the variety of elements present in the proximal hyperspectral image of the vineyard.

In contrast to previous works by Gutiérrez et al. [22] and Benelli et al. [25], the present work split the ROIs up into sun-exposed ('Grapes, sunny') and shaded grapes ('Grapes, shadow'). Additionally, an automatic classification method based on PLS-DA was used. Random selection of 80 RGB images from the entire set of 187 hyperspectral images was performed in order to calculate mean absorbance spectra from the labelled areas of interest (Fig. 4).

The seven-class labelling of the RGB images ('Grapes, sunny', 'Grapes, shadow', 'Leaf, sunny', 'Leaf, shadow', 'Background, grass', 'Background, sky', 'Branches') was simplified by the alignment of the vertical scan lines resulting from the acquisition of the hyperspectral images (Fig. 5): indeed, the up-down shifts on the vertical plane of the hyperspectral camera, mainly due to the roughness on the ground on which the cart was running, resulted in a significant misalignment of the vertical scan lines. 'Overexposed' areas resulting from gamma correction (Fig. 5B) of the RGB images were excluded from the selection of areas of interest.

The best PLS-DA classification models of grapes relative to the aggregated class 'Sunny + Shady' were obtained by pre-processing with smoothing (window: 9) + SNV + MC, and *i*PLS variable selection method (interval size = 50). The PLS-DA model includes 3 latent variables and has a resulting sensitivity and specificity values of 0.991 and 0.996, respectively. However, all PLS-DA models performed well, with number of latent variables between 2 and 8 and with sensitivity and specificity values no lower than 0.983 and 0.960, respectively (Table 1). The same pre-processing applied to the PLS-DA models for the classification of grapes exposed to sun or shade (classes 'Sunny' and 'Shady', respectively) produced slightly inferior results. The best PLS-DA model of grapes exposed to direct solar radiation (class 'Sunny'), using 4 latent variables and *i*PLS interval size = 6, resulted in a sensitivity = 0.988 and specificity = 0.940. Finally, the best PLS-DA model for classification of grapes in shade (class 'Shady'), using 9 latent variables and *i*PLS interval size = 6, resulted in a sensitivity and specificity of 0.920 and 0.927 respectively.

Afterwards, the three PLS-DA classification models reported were used in prediction to define the ROIs of the whole set of hyperspectral images of the vineyard sections. Finally, the mean absorbance spectra of the 6 classes of ROIs obtained, 'Sunny + Shady', 'Sunny', 'Shady', 'Super Sunny + Shady', 'Super Sunny', 'Super Shady', were used to calculate PLS models to predict the °Brix of grapes (Table 2).

The mean absorbance spectra of the grape pixel-based ROIs (classes 'Sunny + Shady', 'Sunny', and 'Shady') obtained by averaging the mean spectra of the respective ROIs of the entire set of hyperspectral images are shown in Fig. 6. Considering the spectral range of the hyperspectral camera adopted (400–1000 nm), the NIR region is particularly interesting for SSC-related spectral information. The second overtone O–H stretching vibration for water is observed at 960–970 nm and for carbohydrates in the 950–1000 nm region; the third overtone of the C–H stretching vibrations is found at around 900 nm. Since the water content of ripe wine grapes is 70–80 % [37], the water-related absorption bands dominate over the carbohydrate-related ones, but it was observed that the water absorption peaks in the NIR spectral region are not very marked and broad, so the carbohydrate-related spectral information should be less covered by the water-related information [38,39].

The best PLS models were obtained with SNV pre-processing and leave-one-day-out cross-validation was adopted to validate the models. The SNV pre-processing was not preceded by smoothing, as in the case of the PLS-DA models, since the calculation of the mean spectra of the ROIs contributed to reduce the high noise level present at the single spectrum level. In particular, the PLS model of the ROIs related to the 'Sunny + Shady' class (using 5 latent variables) resulted in R^2_{CV} = 0.69 and RMSECV = 0.94 °Brix; a similar result was obtained with the 'Super Sunny + Shady' ROIs, with an R^2_{CV} = 0.67 and RMSECV = 0.97 °Brix, using 4 latent variables. These results are comparable to previous PLS prediction results obtained with the ROIs from manual selection, with R^2_{CV} = 0.70 and RMSECV = 0.92 °Brix, but with a much higher number of latent variables (8) (Table 2).

Finally, two variable selection methods, *i*PLS and *r*PLS, were applied to the three PLS models described. *i*PLS proved to be a suitable method for data reduction and localisation of informative spectral regions, thus improving the predictive performance and simplicity of the PLS models. The best PLS model was obtained for the 'Sunny + Shady' ROIs: by using 4 latent variables and *i*PLS interval size = 12, R^2_{CV} = 0.74 and RMSECV = 0.86 °Brix were obtained. Similar results were also achieved with the ROIs 'Super Sunny + Shady': by using 5 latent variables and *i*PLS interval size = 25, R^2_{CV} = 0.74 and RMSECV = 0.86 °Brix were obtained (Fig. 7). These results are comparable with those relative to the manual selection of ROIs: the PLS model, using 6 latent variables and *i*PLS interval size = 6, resulted in R^2_{CV} = 0.73 and RMSECV = 0.87 °Brix (Table 3).

The application of Vis/NIR spectroscopic techniques to predict the SSC of grapes directly in the field has already been reported and described in literature. Using Portable Vis/NIR spectrometers and PLS regression, R^2_{CV} = 0.72 and a standard error of prediction in cross-validation (SEPCV) = 0.61 °Brix [40], correlation coefficient in prediction (r_P) = 0.82 and RMSEP = 1.48 °Brix [41] were obtained. By means of support vector machine regression (SVMR) Gutiérrez et al. [22] obtained R^2_P = 0.92 and RMSEP = 1.274 °Brix. Benelli et al. [25] obtained R^2_{CV} = 0.77 and RMSECV = 0.79 °Brix from the dataset used for the present study, but excluding the days of analysis without clear sky, and by manual selection of the ROIs. The results of the present study are thus comparable with those reported in literature, and in particular the prediction errors, RMSE, obtained are slightly better than those obtained by Gutiérrez et al. [22].

Recently, two studies [42,43] adopted snapshot Vis/NIR hyperspectral cameras directly in the field to assess the °Brix of ripening grapes. Tsakiridis et al. [42] analysed four grape varieties and optimised the grape reflectance spectra by means of a denoising and convolutional autoencoder framework. PLS regression models were developed for each variety, but the results were not particularly accurate, with the best RMSE being 1.66 °Brix. In a study by Swe et al. [43], a °Brix prediction model combined with two machine learning approaches were developed and applied on a grape variety, with the enhanced ridge model producing the best results, achieving an R^2 value of 0.77 and an RMSE of 0.99 °Brix. The snapshot camera has an advantage over line scan cameras as it avoids scan-line misalignment. In this study, manual labelling of areas of interest in RGB images for building the PLS-DA calibration model for classification is complicated by the misalignment of the scanned lines. However, the problem was solved by developing a self-alignment algorithm. Furthermore, it is worth noting that the misalignment has no effect on predicting pixel-based regions of interest. Nevertheless, for future analysis, it is recommended that the push-broom line scan hyperspectral camera be mounted on a gimbal-type three-axis stabilisation system to reduce the misalignment problem, and that an encoder be included on the cart wheelbase synchronised to the camera line scan acquisition. A further limitation of the present study is the need to perform frequent white calibration of the hyperspectral camera on partly cloudy days, when a sudden change in the intensity of the solar radiation could occur. To address this, a possible solution could be to speed up the operation by acquiring a single hyperspectral image per vineyard row, without dividing it into sections, and performing the white calibration before each row scan. In addition, it is not advisable to acquire hyperspectral images in rainy and windy conditions.

Finally, it would be interesting to compare the performance of the pixel-based classification system of regions of interest presented here with techniques based on deep learning [44], particularly convolutional neural networks [45,46], under field conditions characterised by complex backgrounds. It would also be interesting to extend the analysis for comparative purposes to more grape varieties.

4. Conclusions

The present study provided a valid and automatic classification method of the regions of interest for grapes in hyperspectral images of vineyard row sections during post-veraison and up to harvest. The best PLS models were obtained from the aggregated region of interest containing both sunlit and shaded grapes which proved to perform better than the individual ROIs related to sunlit grapes or shaded grapes. Moreover, the mean spectra obtained from the automatic mapping of the regions of interest demonstrated to provide prediction results on par with those obtained by carefully manual selections of the regions of interest using simpler models (fewer PLS components), giving promise of more robust predictions of the maturity of the grapes as measured by the SSC content.

Ethics statement

Not applicable: This manuscript does not include human or animal research.

CRediT authorship contribution statement

Alessandro Benelli: Conceptualization, Methodology, Formal analysis, Writing – original draft. **Chiara Cevoli:** Methodology, Formal analysis. **Angelo Fabbri:** Supervision. **Søren Balling Engelsen:** Conceptualization, Methodology, Supervision. **Klavs Martin Sørensen:** Conceptualization, Methodology, Software.

Declaration of competing interest

The authors declare that they have no known competing financial interests or personal relationships that could have appeared to influence the work reported in this paper.

Data availability

Data will be made available on request.

References

[1] F. Droulia, I. Charalampopoulos, Future climate change impacts on European viticulture: a review on recent scientific advances, Atmosphere 12 (2021) 495, https://doi.org/10.3390/atmos12040495 (Basel).

[2] OIV (International Organisation of Vine and Wine Intergovernmental Organisation), World Wine Production Outlook, First Estimates 4 November 2021, Paris, 2021. https://www.oiv.int/public/medias/8553/en-oiv-2021-world-wine-production-first-estimates-to-update.pdf (accessed November 13, 2021).

[3] M. Keller, Phenology and growth cycle. Science Grapevines, 3rd ed., Academic Press, 2020, pp. 61–103, https://doi.org/10.1016/B978-0-12-816365-8.00002-6.

[4] J.J. Hunter, C.G. Volschenk, E. Mania, A.V. Castro, M. Booyse, S. Guidoni, A. Pisciotta, R. Di Lorenzo, V. Novello, R. Zorer, Grapevine row orientation mediated temporal and cumulative microclimatic effects on grape berry temperature and composition, Agric. For. Meteorol. 310 (2021) 108660, https://doi.org/10.1016/j.agrformet.2021.108660.

[5] P. Romero, J.M. Navarro, P.B. Ordaz, Towards a sustainable viticulture: the combination of deficit irrigation strategies and agroecological practices in Mediterranean vineyards. A review and update, Agric. Water Manag. 259 (2022) 107216, https://doi.org/10.1016/J.AGWAT.2021.107216.

[6] M. Keller, Developmental physiology. Science Grapevines, 3rd ed., Academic Press, 2020, pp. 199–277, https://doi.org/10.1016/B978-0-12-816365-8.00006-3.

[7] L.G. Santesteban, Precision viticulture and advanced analytics. A short review, Food Chem. 279 (2019) 58–62, https://doi.org/10.1016/j.foodchem.2018.11.140.

[8] M. Ammoniaci, S.P. Kartsiotis, R. Perria, P. Storchi, State of the art of monitoring technologies and data processing for precision viticulture, Agriculture 11 (2021) 201, https://doi.org/10.3390/agriculture11030201.

[9] C. Karakizi, M. Oikonomou, K. Karantzalos, Spectral discrimination and reflectance properties of various vine varieties from satellite, UAV and proximate sensors, Int. Arch. Photogramm. Remote Sens. Spat. Inf. Sci. (2015) 31–37, https://doi.org/10.5194/isprsarchives-XL-7-W3-31-2015. XL-7-W3.

[10] J.J. Sousa, P. Toscano, A. Matese, S.F. Di Gennaro, A. Berton, M. Gatti, S. Poni, L. Pádua, J. Hruška, R. Morais, E. Peres, UAV-based hyperspectral monitoring using push-broom and snapshot sensors: a multisite assessment for precision viticulture applications, Sensors 22 (2022) 6574, https://doi.org/10.3390/S22176574, 2022, Vol. 22, Page 6574.

[11] A. Khaliq, L. Comba, A. Biglia, D. Ricauda Aimonino, M. Chiaberge, P. Gay, Comparison of satellite and UAV-based multispectral imagery for vineyard variability assessment, Remote Sens. 11 (2019), https://doi.org/10.3390/rs11040436.

[12] M. Ferrer, G. Echeverría, G. Pereyra, G. Gonzalez-Neves, D. Pan, J.M. Mirás-Avalos, Mapping vineyard vigor using airborne remote sensing: relations with yield, berry composition and sanitary status under humid climate conditions, Precis. Agric. 21 (2020) 178–197, https://doi.org/10.1007/s11119-019-09663-9.

[13] L. Pádua, P. Marques, T. Adão, N. Guimarães, A. Sousa, E. Peres, J.J. Sousa, Vineyard variability analysis through UAV-based vigour maps to assess climate change impacts, Agronomy 9 (2019), https://doi.org/10.3390/agronomy9100581.

[14] L. Pádua, T. Adão, A. Sousa, E. Peres, J.J. Sousa, Individual grapevine analysis in a multi-temporal context using UAV-based multi-sensor imagery, Remote Sens. 12 (2020) 139, https://doi.org/10.3390/RS12010139.

[15] L. Comba, A. Biglia, D.R. Aimonino, P. Barge, C. Tortia, P. Gay, 2D and 3D data fusion for crop monitoring in precision agriculture, in: Proceedings of the 2019 IEEE International Workshop on Metrology for Agriculture and Forestry, IEEE, 2019, pp. 62–67, https://doi.org/10.1109/MetroAgriFor.2019.8909219.

[16] Z. Kandylakis, A. Falagas, C. Karakizi, K. Karantzalos, Water stress estimation in vineyards from aerial SWIR and multispectral UAV data, Remote Sens. 12 (2020) 2499, https://doi.org/10.3390/RS12152499.

[17] J. Bellvert, M. Mata, X. Vallverdú, C. Paris, J. Marsal, Optimizing precision irrigation of a vineyard to improve water use efficiency and profitability by using a decision-oriented vine water consumption model, Precis. Agric. (2021) 319–341, https://doi.org/10.1007/s11119-020-09718-2.

[18] V. Pagay, C.M. Kidman, Evaluating remotely-sensed grapevine (Vitis vinifera L.) water stress responses across a viticultural region, Agronomy 9 (2019) 682, https://doi.org/10.3390/agronomy9110682.

[19] J. Albetis, S. Duthoit, F. Guttler, A. Jacquin, M. Goulard, H. Poilvé, J.B. Féret, G. Dedieu, Detection of flavescence dorée grapevine disease using unmanned aerial vehicle (UAV) multispectral imagery, Remote Sens. 9 (2017) 308, https://doi.org/10.3390/rs9040308.

[20] J. Albetis, A. Jacquin, M. Goulard, H. Poilvé, J. Rousseau, H. Clenet, G. Dedieu, S. Duthoit, On the potentiality of UAV multispectral imagery to detect flavescence Dorée and grapevine trunk diseases, Remote Sens. 11 (2019) 23, https://doi.org/10.3390/rs11010023.

[21] M.A. Musci, C. Persello, A.M. Lingua, UAV images and deep-learning algorithms for detecting flavescence doree disease in grapevine orchards, in: Proceedings of the International Archives of the Photogrammetry, Remote Sensing and Spatial Information Sciences, 2020, pp. 1483–1489, https://doi.org/10.5194/isprs-archives-XLIII-B3-2020-1483-2020.

[22] S. Gutiérrez, J. Tardaguila, J. Fernández-Novales, M.P. Diago, On-the-go hyperspectral imaging for the in-field estimation of grape berry soluble solids and anthocyanin concentration, Aust. J. Grape Wine Res. 25 (2019) 127–133, https://doi.org/10.1111/ajgw.12376.

[23] J. Fernández-Novales, J. Tardáguila, S. Gutiérrez, M.P Diago, On-The-Go VIS + SW − NIR spectroscopy as a reliable monitoring tool for grape composition within the vineyard, Molecules 24 (2019) 2795, https://doi.org/10.3390/molecules24152795.

[24] J. Fernández-Novales, I. Barrio, M.P. Diago, Non-invasive monitoring of berry ripening using on-the-go hyperspectral imaging in the vineyard, Agronomy 11 (2021) 2534, https://doi.org/10.3390/agronomy11122534.

[25] A. Benelli, C. Cevoli, L. Ragni, A. Fabbri, In-field and non-destructive monitoring of grapes maturity by hyperspectral imaging, Biosyst. Eng. 207 (2021) 59–67, https://doi.org/10.1016/j.biosystemseng.2021.04.006.

[26] S. Río Segade, S. Giacosa, V. Gerbi, L. Rolle, Grape maturity and selection: automatic grape selection, A. Morata (Ed.), Red Wine Technol. (2019) 1–16, https://doi.org/10.1016/B978-0-12-814399-5.00001-3.

[27] W. Guo, W. Li, B. Yang, Z.Z. Zhu, D. Liu, X. Zhu, A novel noninvasive and cost-effective handheld detector on soluble solids content of fruits, J. Food Eng. 257 (2019) 1–9, https://doi.org/10.1016/j.jfoodeng.2019.03.022.

[28] K.M. Sørensen, F. van den Berg, S.B. Engelsen, NIR data exploration and regression by chemometrics—a primer, Y. Ozaki, C. Huck, S. Tsuchikawa, S.B. Engelsen (Eds.). Near-Infrared Spectrosc, Springer, Singapore, 2021, pp. 127–189, https://doi.org/10.1007/978-981-15-8648-4_7.

[29] Labelbox, Labelbox, [Online]. (2021). https://labelbox.com/(accessed December 12, 2021).

[30] R.G. Brereton, G.R. Lloyd, Partial least squares discriminant analysis: taking the magic away, J. Chemom. 28 (2014) 213–225, https://doi.org/10.1002/CEM.2609.

[31] Å. Rinnan, F. Berg, S.B. Engelsen, Review of the most common pre-processing techniques for near-infrared spectra, TrAC Trends Anal. Chem. 28 (2009) 1201–1222, https://doi.org/10.1016/j.trac.2009.07.007.

[32] L. Nørgaard, A. Saudland, J. Wagner, J.P. Nielsen, L. Munck, S.B. Engelsen, Interval partial least-squares regression (iPLS): a comparative chemometric study with an example from near-infrared spectroscopy, Appl. Spectrosc. 54 (2000) 413–419. https://www.osapublishing.org/as/abstract.cfm?uri=as-54-3-413. accessed December 18, 2021.

[33] Å. Rinnan, M. Andersson, C. Ridder, S.B. Engelsen, Recursive weighted partial least squares (rPLS): an efficient variable selection method using PLS, J. Chemom. 28 (2014) 439–447, https://doi.org/10.1002/cem.2582.

[34] S. Cubero, M.P. Diago, J. Blasco, J. Tardáguila, B. Millán, N. Aleixos, A new method for pedicel/peduncle detection and size assessment of grapevine berries and other fruits by image analysis, Biosyst. Eng. 117 (2014) 62–72, https://doi.org/10.1016/j.biosystemseng.2013.06.007.

[35] S. Liu, M. Whitty, Automatic grape bunch detection in vineyards with an SVM classifier, J. Appl. Log. 13 (2015) 643–653, https://doi.org/10.1016/j.jal.2015.06.001.
[36] L. Luo, Y. Tang, X. Zou, M. Ye, W. Feng, G. Li, Vision-based extraction of spatial information in grape clusters for harvesting robots, Biosyst. Eng. 151 (2016) 90–104, https://doi.org/10.1016/J.BIOSYSTEMSENG.2016.08.026.
[37] FAO (Food and Agriculture Organization), Grapes Wine - Agribusiness Handbook, Rome, 2009. http://www.fao.org/3/al176e/al176e.pdf.
[38] M. Manley, E. Joubert, L. Myburgh, E. Lotz, M. Kidd, Prediction of soluble solids content and post-storage internal quality of Bulida apricots using near infrared spectroscopy, J. Near Infrared Spectrosc. 15 (2007) 179–188, https://doi.org/10.1255/jnirs.725.
[39] C. Camps, D. Christen, On-tree follow-up of apricot fruit development using a hand-held NIR instrument, J. Food Agric. Environ. 7 (2009) 394–400.
[40] B. Diezma-Iglesias, P. Barreiro, R. Blanco, F.J. García-Ramos, Comparison of robust modeling techniques on NIR spectra used to estimate grape quality, in: Proceedings of the Acta Horticulture International Society for Horticultural Science, 2008, pp. 367–372, https://doi.org/10.17660/ActaHortic.2008.802.48.
[41] R. Guidetti, R. Beghi, L. Bodria, Evaluation of grape quality parameters by a simple VIS/NIR system, in: Proceedings of the Transactions of the ASABE, 2010, pp. 477–484, https://doi.org/10.13031/2013.29556.
[42] N.L. Tsakiridis, N. Samarinas, S. Kokkas, E. Kalopesa, N.V. Tziolas, G.C. Zalidis, *In situ* grape ripeness estimation via hyperspectral imaging and deep autoencoders, Comput. Electron. Agric. 212 (2023) 108098, https://doi.org/10.1016/j.compag.2023.108098.
[43] K.N. Swe, S. Takai, N. Noguchi, Novel approaches for a brix prediction model in Rondo wine grapes using a hyperspectral Camera: comparison between destructive and Non-destructive sensing methods, Comput. Electron. Agric. 211 (2023) 108037, https://doi.org/10.1016/j.compag.2023.108037.
[44] I.H. Sarker, Deep learning: a comprehensive overview on techniques, taxonomy, applications and research directions, SN Comput. Sci. 2 (2021) 1–20, https://doi.org/10.1007/s42979-021-00815-1.
[45] X. He, Y. Chen, P. Ghamisi, Heterogeneous transfer learning for hyperspectral image classification based on convolutional neural network, in: Proceedings of the IEEE Transactions on Geoscience and Remote Sensing, IEEE, 2020, pp. 3246–3263, https://doi.org/10.1109/TGRS.2019.2951445.
[46] J. Zhao, Q. Hu, B. Li, Y. Xie, H. Lu, S. Xu, Research on an improved non-destructive detection method for the soluble solids content in bunch-harvested grapes based on deep learning and hyperspectral imaging, Appl. Sci. 13 (2023), https://doi.org/10.3390/app13116776.